



7-7-2020

## Analytic gradients for state-averaged multiconfiguration pair-density functional theory

Thais R. Scott

Matthew R. Hermes


Andrew M. Sand

Meagan S. Oakley

Donald G. Truhlar

*See next page for additional authors*

Follow this and additional works at: [https://digitalcommons.butler.edu/facsch\\_papers](https://digitalcommons.butler.edu/facsch_papers)

 Part of the [Other Chemistry Commons](#)

---

---

**Authors**

Thais R. Scott, Matthew R. Hermes, Andrew M. Sand, Meagan S. Oakley, Donald G. Truhlar, and Laura Gagliardi

---

# Analytic gradients for state-averaged multiconfiguration pair-density functional theory

Cite as: J. Chem. Phys. **153**, 014106 (2020); <https://doi.org/10.1063/5.0007040>

Submitted: 09 March 2020 . Accepted: 28 May 2020 . Published Online: 07 July 2020

 Thais R. Scott,  Matthew R. Hermes,  Andrew M. Sand,  Meagan S. Oakley,  Donald G. Truhlar, and  Laura Gagliardi



View Online



Export Citation



CrossMark

## ARTICLES YOU MAY BE INTERESTED IN

[Modern quantum chemistry with \[Open\]Molcas](#)

The Journal of Chemical Physics **152**, 214117 (2020); <https://doi.org/10.1063/5.0004835>

[The ORCA quantum chemistry program package](#)

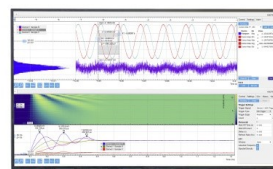
The Journal of Chemical Physics **152**, 224108 (2020); <https://doi.org/10.1063/5.0004608>

[Analytic gradients for multiconfiguration pair-density functional theory with density fitting: Development and application to geometry optimization in the ground and excited states](#)

The Journal of Chemical Physics **154**, 074108 (2021); <https://doi.org/10.1063/5.0039258>

Challenge us.

What are your needs for  
periodic signal detection?



Zurich  
Instruments

# Analytic gradients for state-averaged multiconfiguration pair-density functional theory

Cite as: J. Chem. Phys. 153, 014106 (2020); doi: 10.1063/5.0007040

Submitted: 9 March 2020 • Accepted: 28 May 2020 •

Published Online: 7 July 2020



View Online



Export Citation



CrossMark

Thais R. Scott,<sup>1</sup>  Matthew R. Hermes,<sup>1</sup> Andrew M. Sand,<sup>2</sup>  Meagan S. Oakley,<sup>1</sup>  Donald G. Truhlar,<sup>1,a)</sup>   
and Laura Gagliardi<sup>1,a)</sup> 

## AFFILIATIONS

<sup>1</sup>Department of Chemistry, Chemical Theory Center, and Minnesota Supercomputing Institute, University of Minnesota, Minneapolis, Minnesota 55455, USA

<sup>2</sup>Department of Chemistry and Biochemistry, Butler University, Indianapolis, Indiana 46208, USA

<sup>a)</sup>Authors to whom correspondence should be addressed: [truhlar@umn.edu](mailto:truhlar@umn.edu) and [gagliardi@umn.edu](mailto:gagliardi@umn.edu)

## ABSTRACT

Analytic gradients are important for efficient calculations of stationary points on potential energy surfaces, for interpreting spectroscopic observations, and for efficient direct dynamics simulations. For excited electronic states, as are involved in UV-Vis spectroscopy and photochemistry, analytic gradients are readily available and often affordable for calculations using a state-averaged complete active space self-consistent-field (SA-CASSCF) wave function. However, in most cases, a post-SA-CASSCF step is necessary for quantitative accuracy, and such calculations are often too expensive if carried out by perturbation theory or configuration interaction. In this work, we present the analytic gradients for multiconfiguration pair-density functional theory based on SA-CASSCF wave functions, which is a more affordable alternative. A test set of molecules has been studied with this method, and the stationary geometries and energetics are compared to values in the literature as obtained by other methods. Excited-state geometries computed with state-averaged pair-density functional theory have similar accuracy to those from complete active space perturbation theory at the second-order.

Published under license by AIP Publishing. <https://doi.org/10.1063/5.0007040>

## I. INTRODUCTION

The accurate characterization of electronically excited states is a key element for understanding many chemical processes, with just a few examples being UV damage of DNA,<sup>1-3</sup> *in vivo* imaging of cancer in mice,<sup>4</sup> improving solar cells,<sup>5,6</sup> and photochemical reactions.<sup>7,8</sup> Chemistry involving electronically excited states is also important in many interdisciplinary applications, and it is valuable to use quantum mechanical computations<sup>9,10</sup> to augment what can be learned experimentally about the properties of excited states. Since excited states are usually strongly multiconfigurational, the best results are often obtained by starting with a multiconfigurational reference wave function, such as the wave function obtained by the complete active space self-consistent-field (CASSCF) method.<sup>11,12</sup> CASSCF provides only part of the electron correlation energy, and one must perform further calculations<sup>13</sup>

to obtain accurate properties such as equilibrium geometries and excitation energies. Adding additional correlation energy by excitation into virtual orbitals is usually expensive, but multiconfiguration pair-density functional theory<sup>14,15</sup> (MC-PDFT) avoids this cost by using a density functional instead of including such excitations.

MC-PDFT combines the advantages of Kohn-Sham density functional theory (KS-DFT) and wave function theory. The MC-PDFT method uses an on-top pair-density functional to compute the electronic energy at a reduced cost compared to other approaches yielding energies of similar accuracy to those obtained by second-order complete active space perturbation theory (CASPT2).<sup>16</sup> Studies have shown that both single-state MC-PDFT (SS-PDFT) and state-averaged MC-PDFT (SA-PDFT) almost always have better accuracy than CASSCF or SA-CASSCF, have generally similar accuracy as CASPT2 and sometimes outperform both KS-DFT and CASPT2.<sup>17,18</sup>

Here, we expand the capabilities of SA-PDFT by deriving and implementing analytic gradients of the energy that can be used to determine stationary points on excited-state potential energy surfaces (PESs) or to carry out efficient direct dynamics simulations. Analytic gradients are more efficient than numerical gradients for medium-sized and large molecules (e.g., nucleobases). Additionally, there is no finite difference error when the gradient is computed analytically.

The present work builds on recent work in which SS-PDFT<sup>19</sup> gradients were derived and implemented in *OpenMolcas*.<sup>20</sup> Here, we extend that work to SA-PDFT, and we implement analytic SA-PDFT gradients in both *OpenMolcas* and *mrh*,<sup>21</sup> which is an add-on to *PySCF*.<sup>22</sup> First, the theory and a formal cost scaling analysis of the SA-PDFT gradients are presented. Then, the correctness of the analytic gradients is validated through a comparison to numerical gradients across the potential energy curve for lithium hydride. Finally, the excitation energies and optimized equilibrium geometries for formaldehyde, *trans*-butadiene, and cytosine are reported.

## II. THEORY

In the following text, the indices  $p, q, r, s, t, \dots$  refer to general molecular orbitals (MOs), and  $\kappa, \lambda, \mu, \nu, \dots$  refer to one-electron basis functions, taken here as primitive or contracted Gaussians. The indices  $I, J, K, \dots$  refer to the states included in the average of the SA-CASSCF calculations (this set of states is referred to below as averaged states), and  $R, S, T, \dots$  refer to eigenstates of the Hamiltonian in the complementary part of the active space, referred to as the unaveraged space. The index  $\Lambda$  refers to configuration state functions (CSFs), and the index  $A$  is used for atoms. In practice, it is necessary to partition the MOs into inactive, active, and virtual sets for efficient implementation, but this distinction (and the associated computationally efficient but notationally complex versions of the programmable expressions) is omitted in this section for brevity. Einstein summation notation is used throughout.

### A. SA-PDFT energy

The MC-PDFT energy is

$$E_{\text{MC-PDFT}} = V_n + h_q^p D_q^p + \frac{1}{2} g_{qs}^{pr} D_q^p D_s^r + E_{\text{OT}}[\rho, \rho', \Pi, \Pi'], \quad (1)$$

where  $V_n$ ,  $h_q^p$ , and  $g_{qs}^{pr}$  are the zero-, one-, and two-body Hamiltonian matrix elements;  $D_q^p$  refers to the one-body reduced density matrix for orbitals  $p$  and  $q$ , and  $E_{\text{OT}}$ , which is expressed as a functional of the electronic density,  $\rho$ , the on-top pair density,  $\Pi$ , and their derivatives, is called the on-top energy. The definitions of the electronic density, on-top pair density, and their derivatives are

$$\rho = \phi_p D_q^p \phi_q, \quad (2)$$

$$\rho' = \phi'_p D_q^p \phi_q + \phi_p D_q^p \phi'_q, \quad (3)$$

$$\Pi = \frac{1}{2} \phi_p \phi_q d_{qs}^{pr} \phi_r \phi_s, \quad (4)$$

$$\begin{aligned} \Pi' = \frac{1}{2} & (\phi'_p \phi_q d_{qs}^{pr} \phi_r \phi_s + \phi_p \phi_q d_{qs}^{pr} \phi'_r \phi_s \\ & + \phi_p \phi_q d_{qs}^{pr} \phi'_r \phi_s + \phi_p \phi_q d_{qs}^{pr} \phi_r \phi'_s), \end{aligned} \quad (5)$$

where  $\rho$ ,  $\Pi$ , and  $\phi_p, \phi_q$  are all functions of one three-dimensional real-space coordinate,  $\mathbf{r}$ , and  $\phi_p$  is the  $p$ th molecular orbital. MC-PDFT does not suffer from the “symmetry dilemma”<sup>23,24</sup> of KS-DFT and other single-determinantal methods, in which one must choose between physically realistic spin densities and accurate total energies, because it always involves a reference wave function that is an eigenfunction of  $\hat{S}^2$ , where  $\hat{S}$  is the total electron spin operator.

MC-PDFT uses on-top functionals  $E_{\text{ot}}$  translated from KS exchange–correlation functionals  $E_{\text{xc}}$ <sup>14</sup> such that

$$E_{\text{OT}}[\rho, \Pi, \rho'] = E_{\text{XC}}[\tilde{\rho}_\alpha, \tilde{\rho}_\beta, \tilde{\rho}'_\alpha, \tilde{\rho}'_\beta], \quad (6)$$

where the translation involves fictitious nonphysical spin densities and their derivatives,

$$\tilde{\rho}_\alpha = \begin{cases} \frac{\rho}{2} (1 + \sqrt{1-R}), & R \leq 1 \\ \frac{\rho}{2}, & R > 1, \end{cases} \quad (7)$$

$$\tilde{\rho}_\beta = \begin{cases} \frac{\rho}{2} (1 - \sqrt{1-R}), & R \leq 1 \\ \frac{\rho}{2}, & R > 1, \end{cases} \quad (8)$$

$$\tilde{\rho}'_\alpha = \begin{cases} \frac{\rho'}{2} (1 + \sqrt{1-R}), & R \leq 1 \\ \frac{\rho'}{2}, & R > 1, \end{cases} \quad (9)$$

$$\tilde{\rho}'_\beta = \begin{cases} \frac{\rho'}{2} (1 - \sqrt{1-R}), & R \leq 1 \\ \frac{\rho'}{2}, & R > 1, \end{cases} \quad (10)$$

where  $R$  is also a function of the three-dimensional real-space coordinate  $\mathbf{r}$  and is given by

$$R = \frac{4\Pi}{\rho^2}. \quad (11)$$

Functionals defined as above are called translated and have a prefix “t.” We also use “fully translated” on-top functionals<sup>25</sup> in which the translated densities also depend on the derivatives of  $\Pi$ . These functionals have a prefix “ft” and are not discussed in this work, although the analytic gradients are implemented for both translated and fully translated functionals.

### B. Lagrangian

The Hellmann–Feynman theorem<sup>26,27</sup> implies that if an energy  $E$  is stationary with respect to all parameters defining an underlying wave function, then

$$\frac{\partial E}{\partial \lambda} = \langle \Psi | \frac{\partial \hat{H}}{\partial \lambda} | \Psi \rangle, \quad (12)$$

where  $\Psi$  is the electronic wave function depending on electron coordinates and parametrically on geometric coordinates,  $\hat{H}$  is the Hamiltonian operator, and  $\lambda$  is a geometric coordinate; this allows one to avoid evaluating the response of the wave function to the coordinate change. MC-PDFT is nonvariational, so this cannot be applied, but one can avoid solving for the wave function response to the coordinate change by using Lagrange’s method of undetermined multipliers. The Lagrangian in the SS-PDFT case is

$$\begin{aligned} \mathcal{L}_{\text{MC-PDFT}} &= E_{\text{MC-PDFT}} + \vec{z} \cdot \nabla_{\vec{q}} E_{\text{CASSCF}} \\ &= E_{\text{MC-PDFT}} + \vec{z}_{\text{orb}} \cdot \nabla_{\vec{r}} E_{\text{CASSCF}} + \vec{z}_{\text{CI}} \cdot \nabla_{\vec{p}} E_{\text{CASSCF}}, \end{aligned} \quad (13)$$

where  $\nabla_{\bar{\psi}} E_{\text{CASSCF}}$  is the gradient of the CASSCF energy with respect to the orbital rotations ( $\nabla_{\bar{r}}$ ) and state transfer operators ( $\nabla_{\bar{p}}$ ). The parameterization of the CASSCF energy that allows the evaluation of these derivatives is

$$E_{\text{CASSCF}} = \langle \text{CAS} | \hat{H} | \text{CAS} \rangle, \quad (14)$$

where  $|\text{CAS}\rangle$  is the CASSCF wave function and  $\hat{H}$  is defined as

$$\hat{H} = e^{-\hat{p}} e^{-\hat{k}} \hat{H} e^{\hat{k}} e^{\hat{p}}, \quad (15)$$

$$\hat{k} = \sum_{p < q} \kappa_q^p (\hat{E}_q^p - \hat{E}_p^q), \quad (16)$$

$$\hat{p} = \sum_{\Lambda} P_{\Lambda} (|\Lambda\rangle \langle \text{CAS}| - |\text{CAS}\rangle \langle \Lambda|), \quad (17)$$

where  $\kappa_q^p$  and  $P_{\Lambda}$  are operator amplitudes and  $\hat{E}_q^p$  is the spin-summed excitation operator from the  $q$ th to the  $p$ th orbital. Note that the sum in Eq. (17) is over all CSFs in the active space. Since the CASSCF energy is stationary with respect to the parameters  $\kappa_q^p$  and  $P_{\Lambda}$ , the value of the Lagrangian,  $\mathcal{L}_{\text{MC-PDFT}}$ , is equal to the SS-PDFT energy regardless of the value of the Lagrange multipliers,  $\bar{z}$ . Therefore, one can choose these multipliers such that the Lagrangian is stationary with respect to all wave function parameters by solving [using, for example, the preconditioned conjugate gradient (PCG) method<sup>28</sup>]

$$\nabla_{\bar{\psi}} \mathcal{L}_{\text{MC-PDFT}} = \nabla_{\bar{\psi}} E_{\text{MC-PDFT}} + \mathbf{H}_{\bar{\psi}}^{E_{\text{CAS}}} \cdot \bar{z} = \vec{0}, \quad (18)$$

whereupon the Hellman–Feynman theorem applies to  $\mathcal{L}_{\text{MC-PDFT}}$  and yields the same gradient as full differentiation of  $E_{\text{MC-PDFT}}$ . The gradient vector of the SS-PDFT energy with respect to wave function parameters is  $\nabla_{\bar{\psi}} E_{\text{MC-PDFT}}$ ; it will be called the energy response, and it is discussed in Sec. II C. The term  $\mathbf{H}_{\bar{\psi}}^{E_{\text{CAS}}}$  is the Hessian matrix for the CASSCF energy with respect to wave function parameters.

The generalization of this procedure to the SA-PDFT case is discussed next. In general, the Lagrangian must contain multipliers associated with every parameter that may respond to a change in molecular geometry but with respect to which the energy is not stationary, and these multipliers must have cofactors that accurately represent the conditions determining the values of those parameters. This means that for SA-PDFT, there must be two classes of configuration interaction (CI) transfer parameters that solve different sets of equations. Therefore, we distinguish two kinds of terms in Eq. (17),

$$\hat{p} = \sum_{J,R} P_{JR} (|R\rangle \langle J| - |J\rangle \langle R|) + \sum_{J \neq I} P_{IJ} (|J\rangle \langle I| - |I\rangle \langle J|), \quad (19)$$

where  $I$  indexes the root for which the molecular gradient is sought (and is not summed in the second term),  $|J\rangle$  is an active-space state that appears in the state average, and  $|R\rangle$  is an active-space state that does not appear in the state average (as mentioned at the beginning of Sec. II, these states are called unaveraged states). The orbital parameters ( $\kappa_q^p$ ) and the CI parameters ( $P_{JR}$ ) minimize the SA-CASSCF energy,

$$E_{\text{CASSCF}}^{\text{SA}} = \sum_J \omega_J \langle J | \hat{H} | J \rangle, \quad (20)$$

where  $\omega_J$  is the weight of the  $J$ th root in the state average, and in this work, we assume equal weights in all cases. The SA-CASSCF

energy is insensitive to the CI parameters ( $P_{IJ}$ ) of the averaged states because with the assumption of equal weights it is the trace of a Hermitian matrix under unitary transformation. Instead,  $P_{IJ}$  are chosen to diagonalize the Hamiltonian in the state-averaged space,

$$\langle I | \hat{H} | J \rangle = \delta_{IJ} E_{\text{CASSCF}}^{(I)} \quad \forall J. \quad (21)$$

Comparison of Eqs. (15), (19), and (21) reveals that this is equivalent to a stationarity condition for the  $I$ th root,

$$\frac{\partial E_{\text{CASSCF}}^{(I)}}{\partial P_{IJ}} = \langle I | \hat{H} | J \rangle + \langle J | \hat{H} | I \rangle = 0 \quad \forall J \neq I. \quad (22)$$

Therefore, for the  $I$ th root in SA-PDFT, the Lagrangian is

$$\begin{aligned} \mathcal{L}_{\text{MC-PDFT}}^{(I)} &= E_{\text{MC-PDFT}}^{(I)} + \bar{z}_{\text{orb}} \cdot \nabla_{\bar{r}} E_{\text{CASSCF}}^{\text{SA}} \\ &+ \sum_J \omega_J z_{JR} \frac{\partial E_{\text{CASSCF}}^{(I)}}{\partial P_{JR}} + \sum_{J \neq I} \omega_I z_{IJ} \frac{\partial E_{\text{CASSCF}}^{(I)}}{\partial P_{IJ}} \\ &= E_{\text{MC-PDFT}}^{(I)} + \bar{z}_{\text{orb}} \cdot \nabla_{\bar{r}} E_{\text{CASSCF}}^{\text{SA}} + \sum_J \omega_J \bar{z}_{\text{CI}}^{(J)} \cdot \nabla_{\bar{p}_J} E_{\text{CASSCF}}^{(J)}, \end{aligned} \quad (23)$$

where in the second equality there has been a transformation from the eigenstate to the CSF basis in the second index of  $P_{IJ}$  and  $P_{JR}$ , and the elements of  $\bar{z}_{\text{CI}}^{(J)}$  are

$$z_{J\Lambda} = \begin{cases} \sum_R z_{JR} \langle R | \Lambda \rangle + \sum_K^{n_{\text{SA}}} z_{IK} \langle K | \Lambda \rangle, & J = I \\ \sum_R z_{JR} \langle R | \Lambda \rangle, & \text{otherwise.} \end{cases} \quad (24)$$

Because the coefficient matrix generated by differentiation of Eq. (23) is not symmetric, one cannot apply the PCG method to solve for the values of all Lagrange multipliers in one step. Instead, the linear equations  $\nabla_{\bar{\psi}} \mathcal{L}_{\text{MC-PDFT}}^{(I)} = \vec{0}$  are solved in two steps. First, the insensitivity of the SA energy to  $P_{IJ}$  is exploited to solve analytically for the CI Lagrange multipliers corresponding to averaged states,

$$z_{IJ} = -(E_{\text{CASSCF}}^{(J)} - E_{\text{CASSCF}}^{(I)})^{-1} \frac{1}{2\omega_I} \frac{\partial E_{\text{MC-PDFT}}^{(I)}}{\partial P_{IJ}}, \quad (25)$$

which is possible because the eigenstate basis renders the relevant Hessian matrix diagonal. Second, all other Lagrange multipliers are solved for using the PCG method in the CSF basis,

$$\nabla_{\bar{\psi}} \mathcal{L}_{\text{MC-PDFT}}^{(I)} = \mathbf{P}_{\text{ext}} \cdot \nabla_{\bar{\psi}} E_{\text{MC-PDFT}}^{(I)} + \sum_J \omega_J \mathbf{P}_{\text{ext}} \mathbf{H}_{\bar{\psi}}^{E_{\text{CAS}}^{(J)}} \cdot \bar{z}^{(J)} = \vec{0}, \quad (26)$$

where  $\mathbf{H}_{\bar{\psi}}^{E_{\text{CAS}}^{(J)}}$  is the CASSCF Hessian matrix for the  $J$ th root and  $\bar{z}^{(J)}$  includes both  $\bar{z}_{\text{CI}}^{(J)}$  and the orbital Lagrange multipliers common to all roots,  $\bar{z}_{\text{orb}}$ . The projector matrix,  $\mathbf{P}_{\text{ext}}$ , eliminates all components of CI transfers between states in the average manifold,

$$\{\mathbf{P}_{\text{ext}}\}_{J\Lambda, J'\Lambda'} = 1 - \sum_K^{n_{\text{SA}}} |\Lambda\rangle \langle \Lambda | K \rangle \langle K | \Lambda' \rangle \langle \Lambda' |, \quad (27)$$

thus fixing the  $z_{IJ}$  components at the analytically determined values and preventing any spurious components rotating two averaged roots other than  $I$  ( $z_{JK}$ ) from emerging. Note that the Hessian is projected on only *one* side so that the response of the orbital and

unaveraged CI degrees of freedom to  $z_{IJ}$  is included. In practice, if an implementation of an SA-CASSCF “Hessian” matrix is available, it may not be necessary to include  $\mathbf{P}_{\text{ext}}$  explicitly, but care must be taken to ensure that this matrix is nonsymmetric in the specific way that reproduces Eq. (26) precisely.

### C. Energy response

The Hessian matrix of the CASSCF energy of the  $J$ th root,  $\mathbf{H}_{\Psi}^{E_{\text{CAS}}(J)}$ , is already implemented in many quantum chemistry packages and is not further discussed here. It remains to discuss the PDFT energy response,  $\nabla_{\Psi} E_{\text{MC-PDFT}}^{(I)}$ . The formulas for this response in the SA-PDFT and SS-PDFT cases are essentially the same, and we note that all densities and density matrices that appear in this section in the SA case correspond to the  $I$ th root (not the state average). The overall formulas for the elements of the response (in the CSF basis where applicable) are

$$\frac{\partial E_{\text{MC-PDFT}}}{\partial \kappa_q^p} = F_q^p - F_p^q, \quad (28)$$

$$\frac{\partial E_{\text{MC-PDFT}}}{\partial P_{I\Lambda}} = \langle I | \hat{H}_{\text{ps}} \hat{Q}_I | \Lambda \rangle + \langle \Lambda | \hat{Q}_I \hat{H}_{\text{ps}} | I \rangle, \quad (29)$$

$$\frac{\partial E_{\text{MC-PDFT}}}{\partial P_{J\Lambda}} = 0 \quad \forall J \neq I \quad (30)$$

with

$$F_q^p = (h_r^p + g_{rt}^{ps} D_t^s + V_r^p) D_r^q + v_{rt}^{ps} d_{rt}^{qs}, \quad (31)$$

$$\hat{H}_{\text{ps}} = (h_q^p + g_{qs}^{pr} D_s^r + V_q^p) \hat{E}_q^p + \frac{1}{2} v_{qs}^{pr} \hat{e}_{qs}^{pr}, \quad (32)$$

$$\hat{Q}_I = 1 - |I\rangle\langle I|, \quad (33)$$

where  $V$  and  $v$  are one- and two-body effective potentials, respectively, and  $\hat{e}_{qs}^{pr}$  is the spin-summed two-electron excitation from orbitals  $q, s$  to  $p, r$ . Note that Eq. (29) spans both the averaged and unaveraged spaces [i.e., it contributes to both Eqs. (25) and (26)].

The effective potentials account for the differentiation of the on-top energy. They are

$$V_q^p = \int \frac{\partial \epsilon_{\text{OT}}}{\partial \rho} \phi_p \phi_q + \frac{\partial \epsilon_{\text{OT}}}{\partial \rho'} (\phi_p' \phi_q + \phi_p \phi_q') d\mathbf{r}, \quad (34)$$

$$v_{qs}^{pr} = \int \frac{\partial \epsilon_{\text{OT}}}{\partial \Pi} \phi_p \phi_q \phi_r \phi_s d\mathbf{r}, \quad (35)$$

where  $\epsilon_{\text{OT}}$  is the integrand of the on-top energy with respect to a real-space coordinate,

$$E_{\text{OT}} = \int \epsilon_{\text{OT}}(\mathbf{r}) d\mathbf{r}. \quad (36)$$

As discussed earlier, the on-top functional is a translation of a Kohn–Sham density functional. Therefore, the derivatives of the integrand  $\epsilon_{\text{OT}}$  (collectively  $\nabla_{\vec{\rho}} \epsilon_{\text{OT}}$ ) are obtained via the chain rule,

$$\nabla_{\vec{\rho}} \epsilon_{\text{OT}} = \nabla_{\vec{\rho}} \epsilon_{\text{XC}} \cdot \mathbf{J}_{\vec{\rho}}, \quad (37)$$

where

$$\nabla_{\vec{\rho}} \epsilon_{\text{XC}} = \left\{ \frac{\partial \epsilon_{\text{XC}}}{\partial \bar{\rho}_\alpha}, \frac{\partial \epsilon_{\text{XC}}}{\partial \bar{\rho}_\beta}, \frac{\partial \epsilon_{\text{XC}}}{\partial \bar{\rho}'_\alpha}, \frac{\partial \epsilon_{\text{XC}}}{\partial \bar{\rho}'_\beta} \right\}, \quad (38)$$

and the Jacobian matrix,  $\mathbf{J}_{\vec{\rho}}$ , is

$$\mathbf{J}_{\vec{\rho}} = \begin{pmatrix} \frac{\partial \bar{\rho}_\alpha}{\partial \rho} & \frac{\partial \bar{\rho}_\alpha}{\partial \rho'} & \frac{\partial \bar{\rho}_\alpha}{\partial \Pi} \\ \frac{\partial \bar{\rho}_\beta}{\partial \rho} & \frac{\partial \bar{\rho}_\beta}{\partial \rho'} & \frac{\partial \bar{\rho}_\beta}{\partial \Pi} \\ \frac{\partial \bar{\rho}'_\alpha}{\partial \rho} & \frac{\partial \bar{\rho}'_\alpha}{\partial \rho'} & \frac{\partial \bar{\rho}'_\alpha}{\partial \Pi} \\ \frac{\partial \bar{\rho}'_\beta}{\partial \rho} & \frac{\partial \bar{\rho}'_\beta}{\partial \rho'} & \frac{\partial \bar{\rho}'_\beta}{\partial \Pi} \end{pmatrix}. \quad (39)$$

The quantities in Eq. (38) can be obtained in standard KS-DFT implementations. Those in Eq. (39) are obtained by applying the chain rule to Eqs. (7)–(11) and are tabulated in the [supplementary material](#).

### D. Derivative of the Lagrangian

Given a set of Lagrange multipliers that solve Eqs. (25) and (26), the molecular gradient for the  $I$ th root MC-PDFT energy in SA-PDFT is obtained by differentiating Eq. (23) with respect to nuclear displacements. The chain rule for this operation generates terms involving the derivatives of the Hamiltonian matrix elements, atomic orbital (AO) overlap integrals in a finite AO basis, the on-top energy (including grid coordinates and grid weights in a finite quadrature grid), and density matrices. The last of these are dropped because they are indirect derivatives of wave function parameters, which are constrained to sum to zero by Lagrange’s method of undetermined multipliers.

The derivatives of the Hamiltonian and overlap matrix elements are obtained in the AO basis as

$$h_{\lambda}^{\tilde{\kappa}} \equiv \int \left( \frac{1}{2} \phi_{\kappa} \nabla_{\mathbf{R}_A} \hat{h}_{\text{core}} \phi_{\lambda} - P_{A\kappa} \phi_{\kappa}' \hat{h}_{\text{core}} \phi_{\lambda} \right) d\mathbf{r}, \quad (40)$$

$$g_{\lambda\nu}^{\tilde{\kappa}\mu} \equiv -P_{A\kappa} \int \phi_{\kappa}'(\mathbf{r}_1) \phi_{\lambda}(\mathbf{r}_1) r_{12}^{-1} \phi_{\mu}(\mathbf{r}_2) \phi_{\nu}(\mathbf{r}_2) d\mathbf{r}_1 d\mathbf{r}_2, \quad (41)$$

$$s_{\lambda}^{\tilde{\kappa}} \equiv P_{A\kappa} \int \phi_{\kappa}' \phi_{\lambda} d\mathbf{r}. \quad (42)$$

These equations are essentially first derivatives of the Hamiltonian and overlap matrix elements with respect to the three components of the  $A$ th atomic nucleus’s coordinate,  $\mathbf{R}_A$ . The term  $P_{A\kappa}$  is 1 if  $\kappa$  is an atomic orbital centered on atom  $A$  and 0 otherwise.

The derivatives of the on-top energy can be evaluated in more than one way because they involve tensor products that can be carried out in various orders. Here, we present these derivatives as they are evaluated in our *OpenMolcas* implementation. We generate  $3N_{\text{atom}}$  atomic-coordinate derivatives of the translated densities and their electron-coordinate derivatives (collectively denoted as  $\nabla_{\vec{\lambda}} \vec{\rho}$ ) by using the Jacobian given by Eq. (39) and the atomic-coordinate derivatives of the true density and density derivatives (used in many standard DFT codes) and on-top pair density,

$$\nabla_{\vec{\lambda}} \vec{\rho} = \mathbf{J}_{\vec{\rho}}^{\vec{\rho}} \cdot \nabla_{\vec{\lambda}} \vec{\rho} \quad (43)$$

with

$$\nabla_{\vec{\lambda}} \vec{\rho} = \{ \nabla_{\vec{\lambda}} \bar{\rho}_\alpha, \nabla_{\vec{\lambda}} \bar{\rho}_\beta, \nabla_{\vec{\lambda}} \bar{\rho}'_\alpha, \nabla_{\vec{\lambda}} \bar{\rho}'_\beta \}, \quad (44)$$

$$\nabla_{\tilde{\lambda}} \tilde{\rho} = \{ \nabla_{\tilde{\lambda}} \rho, \nabla_{\tilde{\lambda}} \rho', \nabla_{\tilde{\lambda}} \Pi \}, \quad (45)$$

$$\nabla_{\tilde{\lambda}_A} \rho = -2P_{A\kappa} \phi'_\kappa D_{\tilde{\lambda}}^\kappa \phi_\lambda + P_{Ar} \rho', \quad (46)$$

$$\nabla_{\tilde{\lambda}_A} \rho' = -2P_{A\kappa} (\phi''_\kappa D_{\tilde{\lambda}}^\kappa \phi_\lambda + \phi'_\kappa D_{\tilde{\lambda}}^\kappa \phi'_\lambda) + P_{Ar} \rho'', \quad (47)$$

$$\nabla_{\tilde{\lambda}_A} \Pi = -2P_{A\kappa} \phi'_\kappa \phi_\lambda d_{\lambda\nu}^{\kappa\mu} \phi_\mu \phi_\nu + P_{Ar} \Pi', \quad (48)$$

where  $P_{Ar}$  is 1 if  $\mathbf{r}$  is evaluated at a grid point associated with the  $A$ th atom and 0 otherwise, and the symbol  $\nabla_{\tilde{\lambda}_A}$  in Eqs. (46)–(48) refers to the components of  $\nabla_{\tilde{\lambda}} \rho$ ,  $\nabla_{\tilde{\lambda}} \rho'$ , and  $\nabla_{\tilde{\lambda}} \Pi$ , respectively, which involve the  $A$ th atom. The contribution to the molecular gradient is then evaluated with a standard KS-DFT analytic gradient code,

$$\nabla_{\tilde{\lambda}} E_{\text{OT}} = \int (\nabla_{\tilde{\lambda}} \tilde{\rho} \cdot \nabla_{\tilde{\rho}} \epsilon_{\text{XC}}) d\mathbf{r} + \epsilon_{\text{OT}}(\tilde{\mathbf{r}}) \cdot J_{\tilde{\lambda}}^{\tilde{\omega}}, \quad (49)$$

where the last term accounts for the response of the quadrature weights of the numerical integration (not to be confused with the state-averaged weights of various roots) and corresponds simply to the quadrature evaluation of Eq. (36) with  $3N_{\text{atom}}$  sets of derivatives of quadrature weights in place of the weights themselves.

The details of our *PYSCF* implementation are not presented in detail, but that implementation rearranges the intermediates of Eqs. (43)–(49) to generate derivatives of  $V$  and  $v$  analogous to  $h_{\lambda}^{\tilde{\kappa}}$  and  $g_{\mu\nu}^{\tilde{\kappa}\lambda}$ .

The full expression for the molecular gradient, including the differentiated Hamiltonian, overlap, and on-top contributions, including all finite-grid and finite-basis corrections, is

$$\begin{aligned} \nabla_{\tilde{\lambda}} E_{\text{MC-PDFT}} = & 2[h_q^{\tilde{p}} + g_{qs}^{\tilde{p}r} D_s^r] D_q^{\tilde{p}} + \nabla_{\tilde{\lambda}} E_{\text{OT}} \\ & + 2(h_q^{\tilde{p}} \check{D}_q^{\tilde{p}} + g_{qs}^{\tilde{p}r} \check{d}_{qs}^{\tilde{p}r}) - [s_q^{\tilde{p}} + s_p^{\tilde{q}}] (F_q^{\tilde{p}} + \check{F}_q^{\tilde{p}}), \end{aligned} \quad (50)$$

where  $F_q^{\tilde{p}}$  is from Eq. (31) and

$$\check{F}_q^{\tilde{p}} = h_r^{\tilde{p}} \check{D}_r^{\tilde{q}} + g_{tr}^{\tilde{p}s} \check{d}_{tr}^{\tilde{q}s}. \quad (51)$$

The effective density matrices,  $\check{D}$  and  $\check{d}$ , contain the Lagrange multipliers as follows:

$$\begin{aligned} \check{D}_q^{\tilde{p}} = & \sum_s (\{D_{\text{SA}}\}_q^s z_s^{\tilde{p}} - \{D_{\text{SA}}\}_s^{\tilde{p}} z_q^s) \\ & + \sum_{J,\Lambda} w_J z_{J\Lambda} (\langle \Lambda | \check{E}_q^{\tilde{p}} | J \rangle + \langle J | \check{E}_q^{\tilde{p}} | \Lambda \rangle), \end{aligned} \quad (52)$$

$$\begin{aligned} \check{d}_{qs}^{\tilde{p}r} = & \sum_t (\{d_{\text{SA}}\}_{qs}^{\tilde{p}r} z_t^{\tilde{p}} - \{d_{\text{SA}}\}_{ts}^{\tilde{p}r} z_q^{\tilde{p}} + \{d_{\text{SA}}\}_{qs}^{\tilde{p}t} z_t^{\tilde{r}} - \{d_{\text{SA}}\}_{qt}^{\tilde{p}r} z_s^{\tilde{r}}) \\ & + \sum_{J,\Lambda} w_J z_{J\Lambda} (\langle \Lambda | \check{e}_{qs}^{\tilde{p}r} | J \rangle + \langle J | \check{e}_{qs}^{\tilde{p}r} | \Lambda \rangle), \end{aligned} \quad (53)$$

where  $D_{\text{SA}}$  and  $d_{\text{SA}}$  are the state-averaged one- and two-body density matrices, respectively. All other density matrices appearing in Eq. (50) arise from the differentiation of  $E_{\text{MC-PDFT}}^{(I)}$  and are specific to the  $I$ th root.

### E. Operation cost, storage cost, and timing

Previous work has reported the attractive timing and low memory requirements of MC-PDFT energy computations as compared to

those of CASPT2.<sup>18,29–33</sup> Here, we discuss additional considerations related to timing and memory requirements when one calculates gradients.

The intermediate arrays and tensors that appear above have the same dimensions and sizes as comparable quantities utilized in the evaluation of SA-CASSCF or KS-DFT analytic gradients. The calculations of the two-body effective potential terms ( $v$ ) dominate the overall cost of the SA-PDFT gradient steps, and for these as well as the on-top pair density ( $\Pi$ ) and its various derivatives, we exploit the partition of the MO indices into those for inactive, active, and virtual orbitals. The largest segment of the effective potential or 2-RDM required at any step in the evaluation of SA-PDFT analytic gradients is that which appears in Eq. (31). Here, the block-diagonal structure of the 2-RDM is exploited so that only two-body effective potential elements with at least three indices restricted to the active space are explicitly calculated (this also applies to derivatives of  $v$  alluded to in Sec. II D). This leads to operation and storage costs of  $O(M^1 M_{\text{CAS}}^3 n_{\text{grid}})$  and  $O(M^1 M_{\text{CAS}}^3)$ , respectively, associated with the two-body effective potentials, where  $M$ ,  $M_{\text{CAS}}$ , and  $n_{\text{grid}}$  are the numbers of AOs, active orbitals, and quadrature grid points, respectively. This should be compared to  $O(M^4 M_{\text{CAS}}^1)$  operation and  $O(M^3 M_{\text{CAS}}^1)$  storage costs for the leading step of the integral transformations required in CASSCF without density fitting.

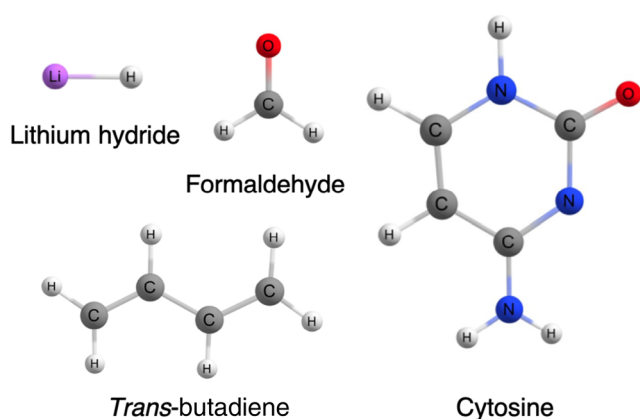
In practice, one usually has  $n_{\text{grid}} \gg M$ , so the two-body effective potential evaluation is often the slowest part of SA-PDFT gradient calculations, including the preceding CASSCF energy calculation. It should also be noted that available memory is used to vectorize the effective potential calculations, so actual memory consumption will often be higher than the minimal “cost” discussed here. Additionally, this analysis ignores the  $O(e^{M_{\text{CAS}}})$  operation and storage cost associated with manipulating the active-space CI vector, which dominates the overall cost of the method in the limit of large  $M_{\text{CAS}}$ .

### III. COMPUTATIONAL METHODS

All SA-PDFT calculations were performed using local versions of *OpenMolcas*<sup>20</sup> and the *PYSCF*<sup>22</sup> add-on package *mrh*<sup>21</sup> using the tPBE on-top functional. Geometry optimizations using energies and gradients computed by *PYSCF* and *mrh* were carried out by the external program *geomeTRIC*.<sup>34</sup> All SA-PDFT computations were performed with the aug-cc-pVTZ basis set and an ultrafine grid size. The CASPT2 geometry optimizations were performed using the same local version of *OpenMolcas* and the 6-311G+(2df) basis set for cytosine. Numerical gradients were computed for CASPT2 since analytic gradients are not yet implemented in *OpenMolcas* or *PYSCF*. The CASPT2 computations were performed with a state-averaged reference wave function, but the PT2 corrections and the PDFT energies were computed independently, and the states were not allowed to interact. For the CASPT2 calculations, the default IPEA shift value, 0.25  $E_h$ , was used, and the default number of frozen deep core orbitals was used for each system studied here. For the numerical gradient in *OpenMolcas*, a  $\Delta$  value of 0.06 was used, and convergence criteria for the orbital rotation matrix and energy gradient were set to  $1.0 \times 10^{-5}$ .

A set of four molecules (shown in Fig. 1) was used to assess the correctness of the analytic gradients and the accuracies of geometries and excitation energies computed with SA-PDFT. All states studied are singlet states.



**FIG. 1.** Systems studied in this work.

The active space used for lithium hydride contains one  $\sigma$  and one  $\sigma^*$  orbital. The active space of formaldehyde is composed of pairs of bonding/antibonding  $\sigma$  (C-H),  $\sigma$  (C=O), and  $\pi$  (C=O) orbitals, oxygen lone pairs, and two second-shell oxygen lone pair orbitals. Two  $\pi$  and two  $\pi^*$  orbitals and the associated electrons are included in the active space for *trans*-butadiene. The active space for cytosine includes the entire occupied  $\pi$  space and lone pair orbitals with three correlating  $\pi^*$  orbitals. Active space sizes, symmetry constraints, number of configurations, and the states included in the average for all molecules studied with SA-PDFT are shown in Table I.

#### IV. RESULTS

We will consider lithium hydride, formaldehyde, and *trans*-butadiene to test the correctness of the analytic gradient implementation, and then, we will consider formaldehyde, *trans*-butadiene, and cytosine to test the accuracy of geometries predicted by SA-PDFT with the newly implemented analytic gradients.

##### A. Correctness of analytic gradients

Gradients were first computed for the ground and first-excited singlet states of LiH to show the agreement between the numerical and analytic gradients. Two low-lying singlet states, namely, the  $X^1\Sigma^+$  and  $A^1\Sigma^+$  states, were considered; we can label the states as  $S_0$  and  $S_1$ . Gradients were computed for both states at 0.1 Å intervals from 0.5 Å to 5.5 Å, and they are shown in Fig. 2 along with the

potential energy curves. The numerical and analytic gradients agree at all distances.

The experimentally determined equilibrium bond distances<sup>35</sup> for the  $X^1\Sigma^+$  and  $A^1\Sigma^+$  states are 1.60 Å and 2.60 Å, respectively. The calculated values are 1.62 Å and 2.91 Å, respectively; the latter does not agree well with experiment. This disagreement is a consequence of the notoriously flat shape of the A state potential well (which is “anomalous” with “a long history”<sup>35</sup>) that arises from an avoided crossing and from severe configuration mixing of valence bond states with ionic, covalent Li 2s, and covalent Li 2p characters;<sup>36,37</sup> the flatness means that a small shift in the energies can be associated with a large shift in the equilibrium distance. To get quantitative results, one should treat the curve crossing region with state-interaction methods including at least three states.<sup>36,37</sup> We note though that the two-state treatment of LiH is not presented here as an attempt to treat this molecule accurately but rather to demonstrate the correctness of the implementation of analytic gradients on a simple case.

The mean unsigned deviation (MUD) for the SA-PDFT analytic gradients compared to the numerical gradients is  $4 \times 10^{-5}$  hartree bohrs<sup>-1</sup>. The same analysis was performed with SA-CASSCF, and the MUD between the analytic and numerical gradients was  $2 \times 10^{-5}$  hartree bohrs<sup>-1</sup>. The analysis for SA-CASSCF is shown in Fig. S1 of the [supplementary material](#). This shows that the SA-PDFT numerical and analytic gradients agree as do the SA-CASSCF analytic and numerical gradients. Further checks involving the SA-PDFT numeric gradients from formaldehyde and *trans*-butadiene are presented in Table S1 of the [supplementary material](#).

##### B. Formaldehyde

Here, optimized geometries for the ground and first-excited singlet states of formaldehyde are compared to experiment and to theoretical structural parameters reported in the work of Budzák, Scalmani, and Jacquemin<sup>9</sup> and references therein. The benchmark dataset includes geometries determined at ADC(2), CC2, CCSD, CCSDR(3), and CC3 levels of theory. Note that the geometries of both the ground and first-excited electronic states are predicted from SA-PDFT calculations based on the same SA-CASSCF active space.

Table II shows that all methods included in this work produce results in good agreement with experiment for the ground-state geometries, and SA-PDFT is the best performing method for the ground state of formaldehyde. In the following text, experimental values are considered as the reference, but it should be noted that a comparison to experiment tests not just SA-PDFT but also other

**TABLE I.** The active spaces, symmetry constraints, number of configuration state functions (CSFs), and number of included states in the state-averaged framework for all systems included in the benchmark study.

System	Active space	Symmetry	States averaged	CSFs
Lithium hydride	(2e, 2o)	None enforced	2	3
Formaldehyde	(12e, 12o)	None enforced	2	226 512
Trans-butadiene	(4e, 4o)	$C_{2h}$	2 ( $^1A_g$ )	12
Cytosine	(14e, 10o)	$C_s$	3 ( $^1A_g$ )	2 598

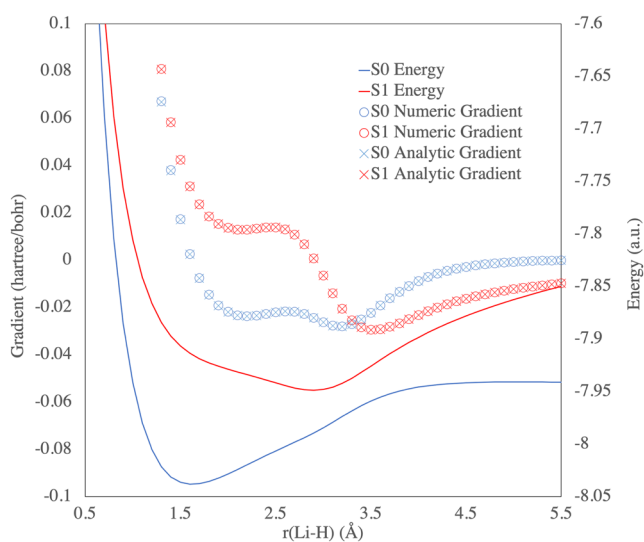


**FIG. 2.** Potential energy surface (PES) scan of lithium hydride from a bond distance of 0.5 Å–5 Å. The numerical and analytic gradients and energies for SA-PDFT are shown at each point on the PES for both the ground,  $S_0$ , and excited,  $S_1$ , states.

factors such as basis set dependence. The geometries optimized with SS-PDFT are also included in this table, but little difference is observed between the SA- and SS-PDFT ground-state geometric parameters.

In order to include both the excited state and the ground state in the same state-averaged manifold in *OpenMolcas*, no spatial symmetry was enforced in the SA-PDFT and SA-CASSCF calculations. However, the geometries computed with CASPT2(12e, 10o) and the single reference methods in Table III [CC2, CCSD, ADC(2), and CC3] imposed  $C_{2v}$  symmetry. Therefore, the energies and geometries were determined using a set of orbitals that are variational with respect to that state's energy and not an average energy. It should be noted that these results are taken from the work by Jacquemin,<sup>13</sup> and it was observed that CC3 and CASPT2 with a large active space and diffuse basis set give geometries close to experiment.<sup>13</sup>

**TABLE II.** Ground-electronic-state equilibrium geometries of formaldehyde with the first row being experiment and the other rows being the difference from the experiment. Bond distances are reported in Å, and angles are reported in degrees.

	C=O	C-H	$\angle$ H-C-H	$\eta$
Expt. <sup>40</sup>	1.208	1.116	116.3	0
SA-PDFT(12e, 12o)	0.002	-0.002	-0.2	0
SS-PDFT(12e, 12o)	0.001	-0.016	0.1	0
CASPT2(12e, 10o) <sup>13</sup>	0.001	-0.014	-0.1	0
SA-CASSCF	0.006	-0.013	1.0	0
ADC(2) <sup>13</sup>	0.002	-0.020	0.2	0
CC2 <sup>13</sup>	0.009	-0.018	0.1	0
CCSD <sup>13</sup>	-0.007	-0.019	0.1	0
CC3	0.000	-0.017	0.2	0

**TABLE III.** Excited-electronic-state equilibrium geometries of formaldehyde with the first row being experiment and the other rows being the difference from the experiment. Bond distances are reported in Å, and angles are reported in degrees.

	C=O	C-H	$\angle$ H-C-H	$\eta$
Expt. <sup>39</sup>	1.323	1.098	118.4	34
SA-PDFT(12e, 12o)	0.000	0.004	-0.8	-6
CASPT2(12e, 10o) <sup>13</sup>	0.003	-0.008	-0.3	4
SA-CASSCF(12e, 12o)	0.033	-0.019	-0.3	-2
ADC(2) <sup>13</sup>	0.057	-0.017	5.4	-15
CC2 <sup>13</sup>	0.030	-0.013	2.9	-5
CCSD <sup>13</sup>	-0.023	-0.011	0.5	-3
CC3 <sup>13</sup>	-0.003	-0.009	-0.2	3

The lowest-lying  $n \rightarrow \pi^*$  state of formaldehyde is known to deviate from a planar structure and to have a significantly lengthened carbonyl bond, and experimental values for the out-of-plane angle,  $\eta$ , vary from 20.5°<sup>38</sup> to 34.0°.<sup>39–41</sup> Here, 34° is taken as the reference value based on both experimental<sup>40,41</sup> and theoretical<sup>13</sup> work. The results computed with SA-PDFT have the second largest error for the puckering angle,  $\eta$ . The carbonyl bond distance for this state is 1.323 Å  $\pm$  0.002 Å,<sup>38–40</sup> which is much longer than the ground state carbonyl bond length of 1.208 Å  $\pm$  0.001 Å.<sup>40,42</sup> Table III shows that SA-PDFT gives results in agreement with experiment for bond distances and  $\angle$  H-C-H for the lowest-lying excited singlet state of formaldehyde.

In Table IV, the adiabatic and vertical energetic gaps are reported for SA-PDFT, CASPT2, and SA-CASSCF. Vertical gaps are computed as the energy difference between the ground and excited states at the optimized ground-state geometry for that method. The adiabatic gaps correspond to the difference in energy computed at the optimized structures for both the excited and ground states for that method. The reference (i.e., the best available estimate that we use for comparison) for the adiabatic gap is CC3<sup>13</sup> and the reference for the vertical gap is experiment.<sup>43</sup> Compared to CC3, the SA-PDFT adiabatic gap is 0.03 eV larger, and the CASPT2 one is 0.02 eV smaller, and SA-CASSCF is 0.01 eV larger. All methods shown here overestimate the experimental vertical gap by more than 0.10 eV; however, SA-PDFT and SA-CASSCF differ from the more expensive CASPT2 by only 0.06 eV.

Formaldehyde was studied in order to compare SA-PDFT geometries and energetics to other methods from the literature, but

**TABLE IV.** The excitation energies between the ground state and lowest-lying excited states with  $^1n \rightarrow \pi^*$  character in formaldehyde.

Method	$\Delta E$ (eV)	
	Adiabatic	Vertical absorption
Expt. <sup>43</sup>		3.79
CC3 <sup>13,44</sup>	3.55	3.97
SA-PDFT(12e, 12o)	3.58	3.92
CASPT2(12e, 10o) <sup>13</sup>	3.53	3.98
SA-CASSCF(12e, 12o)	3.56	4.04

both the ground and first-excited singlet states have single-reference character, and thus, it is not essential to use a multireference method. Next, we consider *trans*-butadiene, which has considerable multireference character.

### C. *Trans*-butadiene

To show the performance of SA-PDFT on a system with a multireference ground state, *trans*-butadiene was studied and compared to results by Watson and Chan.<sup>45</sup> Both the ground state and the  $2^1A_g$  state of *trans*-butadiene are known to have strong multireference character based on their M diagnostics.<sup>46</sup>

The best estimate for the vertical gap has been reported as 6.39  $\pm$  0.07 eV.<sup>45</sup> Multi-state CASPT2 (MS-CASPT2) at the experimental equilibrium geometry predicts the vertical gap to be 6.69 eV.<sup>46</sup> CASPT2 computed for a SA-CASSCF reference wave function with no state interaction is also an interesting comparison to SA-PDFT because SA-PDFT does not include state-interaction effects; therefore, we compare to CASPT2 results as well as MS-CASPT2. The adiabatic, vertical absorption, and vertical de-excitation gaps are shown in Table V.

SA-CASSCF predicts a vertical absorption gap closest to the best estimate, but all methods overestimate the gap by more than 0.15 eV. SA-PDFT is the furthest from this value with a difference of 0.52 eV. For the adiabatic gap, SA-PDFT is 0.09 eV different from the CASPT2 value, while SA-CASSCF differs by 0.26 eV. The vertical de-excitation energy computed with SA-PDFT is 0.08 eV different from CASPT2, and SA-CASSCF is 0.33 eV different from CASPT2. The geometries predicted by these three methods for the ground and excited  $1^1A_g$  states of *trans*-butadiene are shown in Table VI.

For the ground state, all three methods predict geometric parameters that are similar to the reference values. The method with the largest deviation from the experimental value for the C-C bond length is CASPT2, for the  $\angle$ C-C=C angle is SA-CASSCF, and for the C=C bond lengths is SA-PDFT. In the excited state, CASPT2, SA-PDFT, and SA-CASSCF are in excellent agreement.

### D. Cytosine

In this section, we report the optimization of the geometries of the ground and excited states of cytosine; we compare the results to CCSD and MS-CASPT2 computations reported by Fogarasi<sup>48</sup> and

**TABLE VI.** Bond lengths and geometries of the  $1^1A_g$  and  $2^1A_g$  states of *trans*-butadiene with the first set of values being the reference values and the other sets being differences from the reference values. The bond lengths are reported in angstroms (Å), and bond angles are reported in degrees.

Method	$1^1A_g$			$2^1A_g$		
	C=C	C-C	$\angle$ C-C=C	C-C	C=C	$\angle$ C-C=C
Expt. <sup>47</sup>	1.349	1.465	123.8			
CASPT2	-0.007	-0.011	-0.2	1.488	1.394	122.1
SA-PDFT	-0.013	0.005	0.3	0.008	0.003	2.0
SA-CASSCF	-0.004	-0.009	0.5	0.001	0.019	1.1

Nakayama *et al.*,<sup>49</sup> respectively. Cytosine shows the efficiency of SA-PDFT compared with CASPT2 in handling conjugated systems with midsize active spaces. The geometry was optimized with the (14e, 10o) active space, which contains the occupied  $\pi$  space, two lone pair orbitals, and three correlating  $\pi^*$  orbitals and has shown to be accurate in previous work.<sup>50-52</sup> In the SA-PDFT and CCSD/TZP<sup>48</sup> geometry optimizations,  $C_s$  symmetry was used, and the three lowest  $1^1A'$  states were considered. For direct comparison with the SA-PDFT results, cytosine was also optimized with SA(3)-CASSCF(14e, 10o) and CASPT2(14e, 10o), with the same state-averaged reference wave function as used for the SA-PDFT computation. Atomic labels on cytosine are shown in Fig. 3 for use in tabulating and discussing the results (Tables VII-IX).

In Tables VII and VIII, the ground-state geometries of cytosine computed with SA(3)-CASSCF, SA(3)-PDFT, CASPT2(14e, 10o), and CCSD are compared to experiment. The computational entries in these tables are reported as differences with respect to the experimental reference geometry. The SA-PDFT method reproduces the experimental geometry to within 0.06 Å. In some instances, namely, the C1-N2 and N2-C3 bond lengths, SA(3)-PDFT performs slightly

**TABLE V.** The excitation energy (in eV) of the  $2^1A_g$  states in *trans*-butadiene.

Method	$\Delta E$ (eV)		
	Adiabatic	Vertical absorption	Vertical de-excitation <sup>a</sup>
Best estimate <sup>45</sup>		6.39	
MS-CASPT2		6.69	
CASPT2	5.68	6.68	-4.80
SA-PDFT	5.77	6.91	-4.72
SA-CASSCF	5.42	6.57	-4.47

<sup>a</sup>Difference between the ground and  $2^1A_g$  states at the  $2^1A_g$  equilibrium geometry.

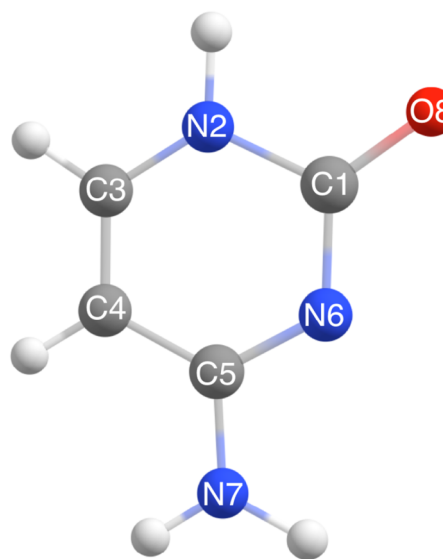


**FIG. 3.** The ground-state geometry of cytosine as optimized by SA(3)-PDFT.

**TABLE VII.** Experimental bond distances (first row in Å) of the ground state of cytosine and differences of theoretical values from experiment.

Method	C1-N2	N2-C3	C3-C4	C4-C5	C5-N7	C5-N6	N6-C1	C1-O8	MUD
Expt. <sup>53</sup>	1.374	1.357	1.342	1.424	1.330	1.337	1.364	1.234	...
SA(3)-CASSCF(14e, 10o)	0.017	-0.003	0.004	0.022	0.020	-0.046	0.027	-0.038	0.02
CCSD <sup>48</sup>	0.042	0.003	0.011	0.022	0.027	-0.024	0.015	-0.020	0.02
CASPT2(14e, 10o)	0.046	0.005	0.015	0.019	0.030	-0.017	0.014	-0.012	0.02
SA(3)-PDFT(14e, 10o)	0.066	-0.017	0.016	0.012	0.021	-0.011	0.000	-0.019	0.02

**TABLE VIII.** Experimental bond angles (first row in degrees) of the ground state of cytosine and differences of theoretical values from experiment.

Method	∠6-1-2	∠5-6-1	∠4-5-6	∠3-2-1	∠3-4-5	∠4-3-2	∠8-1-2	∠8-1-6	∠7-5-6	∠7-5-4	MUD
Expt. <sup>53</sup>	118.1	119.9	122.0	122.7	117.3	120.1	119.8	122.2	118.2	119.9	
SA(3)-CASSCF(14e, 10o)	-1.2	0.6	1.4	0.4	-1.1	-0.2	-0.2	1.4	0.2	-1.8	0.9
CCSD <sup>48</sup>	-1.6	-0.2	2.5	0.8	-1.5	-0.1	-1.1	2.6	-1.0	-1.6	1.3
CASPT2(14e, 10o)	-1.8	-0.2	2.7	1.0	-1.6	-0.2	-1.1	2.8	-1.3	-1.5	1.4
SA(3)-PDFT(14e, 10o)	-2.3	0.6	2.0	0.7	-1.6	-0.5	-2.3	4.5	-1.8	-0.4	1.6

worse than CCSD and CASPT2(14e, 10o). The C1-N2 bond length predicted by SA(3)-PDFT is 0.02 Å longer than the one predicted by CCSD and CASPT2(14e, 10o), 0.049 Å longer than the SA(3)-CASSCF result, and a total of 0.066 Å longer than experiment. For the N2-C3 bond length, SA-PDFT predicts this parameter to be 0.02 Å shorter than experiment, whereas the CCSD and CASPT2(14e, 10o) values are approximately 0.01 Å longer than experiment. The SA(3)-CASSCF results also predict a slightly shorter N2-C3 bond distance than experiment. For other carbon–nitrogen bonds, SA(3)-PDFT gives results similar or closer to experiment than the other methods, as reported in Table VII. The C5-N6 and C5-N7 bonds computed with SA(3)-PDFT have an error 50% smaller compared to CCSD and CASPT2(14e, 10o). The N6-C1 bond length computed with SA(3)-PDFT correctly reproduces the experimental length by up to three decimal places. The SA(3)-CASSCF and SA(3)-PDFT results over- or underestimate the experimental geometry for each bond distance for cytosine, which results in the same sign of error in each case in Table VII. The computed ground state cytosine bond lengths are very similar to the experimental values; each method reported in Table VII [SA(3)-CASSCF(14e, 10o), CCSD, CASPT2(14e, 10o), and SA(3)-PDFT] has a MUD of 0.02 Å.

Table VIII reports the SA(3)-CASSCF, CCSD, CASPT2(14e, 10o), and SA(3)-PDFT bond angle deviations with respect to the

experimental values. All methods have a similar magnitude of error, except for a few angles with larger error from SA(3)-PDFT results. The MUD for SA(3)-CASSCF is 0.9°, CCSD is 1.3°, CASPT2(14e, 10o) is 1.4°, and SA(3)-PDFT is 1.6°. Along with the bond distance analysis above, these data show that SA(3)-PDFT provides a similar accuracy for ground state geometry optimization as CASPT2(14e, 10o) and CCSD.

The geometry of the first-singlet excited state of cytosine was optimized with SA(3)-CASSCF, SA(3)-PDFT, and CASPT2(14e, 10o). The reference CASPT2(14e, 10o) computation used the same active space and number of roots as the SA(3)-PDFT computation. A previous study on the excited states of cytosine provided a MS(2)-CASPT2(8e, 7o) optimized geometry, which is used here as another set of structural parameters to compare to.<sup>49</sup> The active space used was (8e, 7o) and was composed of only  $\pi$  and  $\pi^*$  orbitals. Only two roots were considered in the geometry optimization, and the DZP basis set was used. Each excited state geometry reported in Table IX is of  $^1\pi\pi^*$  character with a final electronic state of  $^1A'$ .

The excited state optimized structure is very similar across all methods. The deviations from CASPT2(14e, 10o) of MS(2)-CASPT2(8e, 7o) and SA(3)-PDFT are of similar magnitude. However, the SA(3)-PDFT geometries deviate slightly in some cases.

**TABLE IX.** CASPT2(14e, 10o) computed bond distances (first row in Å) of the first-singlet excited state of cytosine and differences of subsequent theoretical values from CASPT2(14e, 10o).

Method	C1-N2	N2-C3	C3-C4	C4-C5	C5-N7	C5-N6	N6-C1	C1-O8	MUD
CASPT2(14e, 10o)	1.453	1.301	1.394	1.444	1.350	1.320	1.374	1.210	
SA(3)-CASSCF(14e, 10o)	-0.095	0.080	0.030	-0.079	0.022	0.097	-0.100	0.118	0.08
MS(2)-CASPT2(8e, 7o) <sup>49</sup>	-0.043	0.075	0.036	-0.053	0.047	0.031	-0.049	0.066	0.05
SA(3)-PDFT(14e, 10o)	-0.024	0.081	0.022	-0.059	0.019	0.096	-0.032	0.026	0.04

The SA(3)-CASSCF geometries have the same error or deviate more with respect to the reference geometry than that of SA(3)-PDFT. This shows that SA(3)-PDFT improves the first-excited state geometry of cytosine as compared to SA-CASSCF and ultimately results in a structure closer to that of CASPT2. The MUD from the CASPT2(14e, 10o) excited structure is 0.04 Å for the SA(3)-PDFT results, which is smaller than that of MS(2)-CASPT2(8e, 7o) at 0.05 Å and SA(3)-CASSCF at 0.08 Å.

## V. CONCLUSION

In this work, SA-PDFT analytic gradients were derived and implemented using a Lagrangian framework. This is a generalization of the SS-PDFT analytic gradients previously available in *OpenMolcas*. A test set of four molecules was studied in order to assess the correctness and accuracy of the SA-PDFT gradients, excitation and emission energies, and geometries.

Comparison to numerical gradients for the potential energy curve of LiH and additional comparisons for formaldehyde and *trans*-butadiene showed that SA-PDFT analytic gradients closely agree with numerical SA-PDFT gradients in both the ground state and the first-singlet excited state.

The geometries computed with SA-PDFT are comparable to those computed with CC2, CCSD, CC3, and CASPT2. Analytic gradients for SA-PDFT provide an avenue for the study of excited geometries and excitation energies in systems that are prohibitively expensive when using other post-CASSCF methods. The results presented in this and previous work clearly show that SA-PDFT gives results with similar accuracy to CASPT2 for ground and excited state properties of small organic molecules at an attractive computational cost. In future studies, in order to efficiently optimize geometries of larger molecules, the SA-PDFT gradient expressions will be modified to make use of the density fitting<sup>54,55</sup> approximation to speed up the two-electron integrals.

## SUPPLEMENTARY MATERIAL

See the [supplementary material](#) for the explicit Jacobian matrix elements for the evaluation of the SA-PDFT gradients, analytic and numerical gradients at 0.5 Å intervals on the potential energy curve of LiH using SA-CASSCF, and total energies for the optimized structures using the analytic gradients, and the bond lengths and angles computed using the numerical gradients.

## ACKNOWLEDGMENTS

This work was supported by the National Science Foundation under Grant No. CHE-1764186. The authors acknowledge Minnesota Supercomputing Institute (MSI) at the University of Minnesota for providing resources that contributed to the research results reported within this paper. T.R.S. acknowledges that this material is also based upon work supported by the National Science Foundation Graduate Research Fellowship Program under Grant No. CON-75851, Project No. 00074041. Any opinions, findings, and conclusions or recommendations expressed in this material are those of the author(s) and do not necessarily reflect the views of the National Science Foundation.

## APPENDIX: ERRORS IN REF. 19

We note two misprints and one omission in the derivation of the SS-PDFT gradient reported in Ref. 19. These misprints and omission do not correspond to any errors in the previous code; the previous code was correct.

First, the on-top pair density,  $\Pi$ , defined here by Eq. (4), is incorrectly presented in Eq. (9) of Ref. 19 as

$$\Pi = \phi_p \phi_q d_{qs}^{pr} \phi_r \phi_s, \quad (\text{A1})$$

using the notation of this work. The error is the omission of a factor of 1/2 from Eq. (4).

Second, the programmable equation for the gradient, reported here in Eq. (50), is incorrectly presented in Eq. (68) of Ref. 19 as

$$\begin{aligned} \nabla_{\lambda} E_{\text{MC-PDFT}} = & 2(h_q^{\hat{p}} D_q^p + g_{qs}^{\hat{p}r} d_{qs}^{pr}) + \nabla_{\lambda} E_{\text{OT}} \\ & + 2(h_q^{\hat{p}} \check{D}_q^p + g_{qs}^{\hat{p}r} \check{d}_{qs}^{pr}) - [s_q^{\hat{p}} + s_p^{\hat{q}}](F_q^p + \check{F}_q^p), \end{aligned} \quad (\text{A2})$$

again using this work's notation and conventions. The error is that the product  $D_q^p D_s^r$  in the second term within the first pair of brackets on the right-hand side of Eq. (50) is replaced with the 2-RDM,  $d_{qs}^{pr}$ , which is incorrect because  $g_{qs}^{\hat{p}r} (d_{qs}^{pr} - D_q^p D_s^r)$  corresponds to the derivative of the non-Coulomb contribution to the CASSCF two-electron interaction energy and should not be included in a PDFT gradient expression.

The omission is that the content of Eqs. (43)–(49) is not presented at all in Ref. 19. Instead, Ref. 19 states that  $\nabla_{\lambda} E_{\text{OT}}$  “is evaluated using standard DFT techniques using the translated densities in the evaluation of the derivative of the KS-DFT functional.” This statement is true in that  $3N_{\text{atom}}$  derivatives of the translated densities and density derivatives (i.e.,  $\nabla_{\lambda} \tilde{\rho}$ ) are computed, but Ref. 19 does not present those derivatives or their programmable equations.

## DATA AVAILABILITY

The data that support the findings of this study are available within the article and its [supplementary material](#).

## REFERENCES

- 1 A. L. Sobolewski, W. Domcke, C. Dedonder-Lardeux, and C. Jouvet, “Excited-state hydrogen detachment and hydrogen transfer driven by repulsive  $^1\pi\sigma^*$  states: A new paradigm for nonradiative decay in aromatic biomolecules,” *Phys. Chem. Chem. Phys.* **4**, 1093–1100 (2002).
- 2 F. Plasser, A. J. Aquino, H. Lischka, and D. Nachtigallová, “Electronic excitation processes in single-strand and double-strand DNA: A computational approach,” in *Photoinduced Phenomena in Nucleic Acids II* (Springer, 2014), pp. 1–37.
- 3 R. Improta, F. Santoro, and L. Blancafort, “Quantum mechanical studies on the photophysics and the photochemistry of nucleic acids and nucleobases,” *Chem. Rev.* **116**, 3540–3593 (2016).
- 4 S. T. Adams and S. C. Miller, “Beyond D-luciferin: Expanding the scope of bioluminescence imaging *in vivo*,” *Curr. Opin. Chem. Biol.* **21**, 112–120 (2014).
- 5 K. Andersson, P. A. Malmqvist, B. O. Roos, A. J. Sadlej, and K. Wolinski, “Solar energy conversion by dye-sensitized photovoltaic cells,” *J. Phys. Chem.* **44**, 6841–6851 (2005).
- 6 A. Zhugayevych and S. Tretiak, “Theoretical description of structural and electronic properties of organic photovoltaic materials,” *Annu. Rev. Phys. Chem.* **66**, 305–330 (2015).
- 7 W. G. Dauben, L. Salem, and N. J. Turro, “Classification of photochemical reactions,” *Acc. Chem. Res.* **8**, 41–54 (1975).

- <sup>8</sup>M. Oelgemöller and N. Hoffmann, "Studies in organic and physical photochemistry—An interdisciplinary approach," *Org. Biomol. Chem.* **14**, 7392–7442 (2016).
- <sup>9</sup>Š. Budžák, G. Scalmani, and D. Jacquemin, "Accurate excited-state geometries: A CASPT2 and coupled-cluster reference database for small molecules," *J. Chem. Theory Comput.* **13**, 6237–6252 (2017).
- <sup>10</sup>S. Matsika and A. I. Krylov, "Introduction: Theoretical modeling of excited state processes," *Chem. Rev.* **118**, 6925–6926 (2018).
- <sup>11</sup>B. O. Roos, P. R. Taylor, and P. E. M. Siegbahn, "A complete active space SCF method (CASSCF) using a density matrix formulated super-CI approach," *Chem. Phys.* **48**, 157–173 (1980).
- <sup>12</sup>B. O. Roos, "The complete active space self-consistent field method and its applications in electronic structure calculations," *Adv. Chem. Phys.* **69**, 399–445 (1987).
- <sup>13</sup>D. Jacquemin, "What is the key for accurate absorption and emission calculations, energy or geometry?," *J. Chem. Theory Comput.* **14**, 1534–1543 (2018).
- <sup>14</sup>G. Li Manni, R. K. Carlson, S. Luo, D. Ma, J. Olsen, D. G. Truhlar, and L. Gagliardi, "Multiconfiguration pair-density functional theory," *J. Chem. Theory Comput.* **10**, 3669–3680 (2014).
- <sup>15</sup>L. Gagliardi, D. G. Truhlar, G. Li Manni, R. K. Carlson, C. E. Hoyer, and J. L. Bao, "Multiconfiguration pair-density functional theory: A new way to treat strongly correlated systems," *Acc. Chem. Res.* **50**, 66–73 (2016).
- <sup>16</sup>J. Finley, P.-Å. Malmqvist, B. O. Roos, and L. Serrano-Andrés, "The multi-state CASPT2 method," *Chem. Phys. Lett.* **288**, 299–306 (1998).
- <sup>17</sup>S. Ghosh, P. Verma, C. J. Cramer, L. Gagliardi, and D. G. Truhlar, "Combining wave function methods with density functional theory for excited states," *Chem. Rev.* **118**, 7249–7292 (2018).
- <sup>18</sup>S. J. Stoneburner, D. G. Truhlar, and L. Gagliardi, "MC-PDFT can calculate singlet–triplet splittings of organic diradicals," *J. Chem. Phys.* **148**, 064108 (2018).
- <sup>19</sup>A. M. Sand, C. E. Hoyer, K. Sharkas, K. M. Kidder, R. Lindh, D. G. Truhlar, and L. Gagliardi, "Analytic gradients for complete active space pair-density functional theory," *J. Chem. Theory Comput.* **14**, 126–138 (2018).
- <sup>20</sup>I. F. Galván, M. Vacher, A. Alavi, C. Angeli, F. Aquilante, J. Autschbach, J. J. Bao, S. I. Bokarev, and N. A. Bogdanov, "OpenMolcas: From source code to insight," *J. Chem. Theory Comput.* **15**, 5925–5964 (2019).
- <sup>21</sup>M. R. Hermes, *mrh*, 2020, see <https://github.com/MatthewRHermes/mrh>.
- <sup>22</sup>Q. Sun, T. C. Berkelbach, N. S. Blunt, G. H. Booth, S. Guo, Z. Li, J. Liu, J. D. McClain, E. R. Sayfutyarova, S. Sharma, S. Wouters, and G. K. L. Chan, "PySCF: The python-based simulations of chemistry framework," *Wiley Interdiscip. Rev.: Comput. Mol. Sci.* **8**, e1340 (2018).
- <sup>23</sup>J. P. Perdew, A. Savin, and K. Burke, "Escaping the symmetry dilemma through a pair-density interpretation of spin-density functional theory," *Phys. Rev. A* **51**, 4531 (1995).
- <sup>24</sup>I. G. Kaplan, "Problems in DFT with the total spin and degenerate states," *Int. J. Quantum Chem.* **107**, 2595–2603 (2007).
- <sup>25</sup>R. K. Carlson, D. G. Truhlar, and L. Gagliardi, "Multiconfiguration pair-density functional theory: A fully translated gradient approximation and its performance for transition metal dimers and the spectroscopy of  $\text{Re}_2\text{Cl}_8^{2-}$ ," *J. Chem. Theory Comput.* **11**, 4077–4085 (2015).
- <sup>26</sup>H. Hellmann, *Einführung in die Quantenchemie* (Franz Deuticke, 1937).
- <sup>27</sup>R. P. Feynman, "Forces in molecules," *Phys. Rev.* **56**, 340–343 (1939).
- <sup>28</sup>W. H. Press, S. A. Teukolsky, W. T. Vetterling, and B. P. Flannery, *Numerical Recipes in Fortran 77: The Art of Scientific Computing*, 2nd ed. (Cambridge University Press, Cambridge, UK, 1992).
- <sup>29</sup>J. L. Bao, A. M. Sand, L. Gagliardi, and D. G. Truhlar, "Correlated-participating-orbitals pair-density functional method and application to multiplet energy splittings of main-group divalent radicals," *J. Chem. Theory Comput.* **12**, 4274–4283 (2016).
- <sup>30</sup>K. Sharkas, L. Gagliardi, and D. G. Truhlar, "Multiconfiguration pair-density functional theory and complete active space second order perturbation theory. bond dissociation energies of FeC, NiC, FeS, NiS, FeSe, and NiSe," *J. Phys. Chem. A* **121**, 9392–9400 (2017).
- <sup>31</sup>A. M. Sand, D. G. Truhlar, and L. Gagliardi, "Efficient algorithm for multi-configuration pair-density functional theory with application to the heterolytic dissociation energy of ferrocene," *J. Chem. Phys.* **146**, 034101 (2017).
- <sup>32</sup>M. S. Oakley, J. J. Bao, M. Klobukowski, D. G. Truhlar, and L. Gagliardi, "Multireference methods for calculating the dissociation enthalpy of tetrahedral  $\text{P}_4$  to two  $\text{P}_2$ ," *J. Phys. Chem. A* **122**, 5742–5749 (2018).
- <sup>33</sup>D. Presti, D. G. Truhlar, and L. Gagliardi, "Intramolecular charge transfer and local excitation in organic fluorescent photoredox catalysts explained by RASCI-PDFT," *J. Phys. Chem. C* **122**, 12061–12070 (2018).
- <sup>34</sup>L.-P. Wang and C. Song, "Geometry optimization made simple with translation and rotation coordinates," *J. Chem. Phys.* **144**, 214108 (2016).
- <sup>35</sup>W. C. Stwalley and W. T. Zemke, "Spectroscopy and structure of the lithium hydride diatomic molecules and ions," *J. Phys. Chem. Ref. Data* **22**, 87–112 (1993).
- <sup>36</sup>S. A. Adelman and D. R. Herschbach, "Asymptotic approximation for ionic-covalent configuration mixing in hydrogen and alkali hydrides," *Mol. Phys.* **33**, 793–809 (1977).
- <sup>37</sup>C. E. Hoyer, X. Xu, D. Ma, L. Gagliardi, and D. G. Truhlar, "Diabatization based on the dipole and quadrupole: The DQ method," *J. Chem. Phys.* **141**, 114104 (2014).
- <sup>38</sup>V. A. Job, V. Sethuraman, and K. K. Innes, "The  $3500 \text{ \AA}^1\text{A}_2\text{-}\tilde{\text{X}}^1\text{A}_1$  transition of formaldehyde- $\text{h}_2$ ,  $\text{d}_2$ , and  $\text{hd}$ : Vibrational and rotational analyses," *J. Mol. Spectrosc.* **30**, 365–426 (1969).
- <sup>39</sup>P. Jensen and P. R. Bunker, "The geometry and the inversion potential function of formaldehyde in the  $\tilde{\text{A}}^1\text{A}_2$  and  $\tilde{\text{a}}^3\text{A}_2$  electronic states," *J. Mol. Spectrosc.* **94**, 114–125 (1982).
- <sup>40</sup>D. J. Clouthier and D. A. Ramsay, "The spectroscopy of formaldehyde and thioformaldehyde," *Annu. Rev. Phys. Chem.* **34**, 31–58 (1983).
- <sup>41</sup>I. A. Godunov, A. V. Abramov, V. A. Bataev, and V. I. Pupyshev, "Potential functions of inversion of  $\text{R}_2\text{CO}$  ( $\text{R} = \text{H}, \text{F}, \text{Cl}$ ) molecules in the lowest excited electronic states," *Russ. Chem. Bull.* **48**, 640–646 (1999).
- <sup>42</sup>V. T. Jones and J. B. Coon, "Rotational constants and geometrical structure of the  $^1\text{A}_2$  and  $^3\text{A}_2$  states of  $\text{H}_2\text{CO}$  and  $\text{D}_2\text{CO}$ ," *J. Mol. Spectrosc.* **31**, 137–154 (1969).
- <sup>43</sup>K. N. Walz, C. F. Koerting, and A. Kuppermann, "Electron-impact spectroscopy of acetaldehyde," *J. Chem. Phys.* **87**, 3796–3803 (1987).
- <sup>44</sup>P.-F. Loos, A. Scemama, A. Blondel, Y. Garniron, M. Caffarel, and D. Jacquemin, "A mountaineering strategy to excited states: Highly accurate reference energies and benchmarks," *J. Chem. Theory Comput.* **14**, 4360–4379 (2018).
- <sup>45</sup>M. A. Watson and G. K.-L. Chan, "Excited states of butadiene to chemical accuracy: Reconciling theory and experiment," *J. Chem. Theory Comput.* **8**, 4013–4018 (2012).
- <sup>46</sup>Y. Shu and D. G. Truhlar, "Doubly excited character or static correlation of the reference state in the controversial  $2^1\text{A}_g$  state of *trans*-butadiene?," *J. Am. Chem. Soc.* **139**, 13770–13778 (2017).
- <sup>47</sup>W. Haugen and M. Trætteberg, "Molecular structures of 1,3-butadiene and 1,3,5-*trans*-hexatriene," *Acta Chem. Scand.* **20**, 1726 (1966).
- <sup>48</sup>G. Fogarasi, "Relative stabilities of three low-energy tautomers of cytosine: A coupled cluster electron correlation study," *J. Phys. Chem. A* **106**, 1381–1390 (2002).
- <sup>49</sup>A. Nakayama, S. Yamazaki, and T. Taketsugu, "Quantum chemical investigations on the nonradiative deactivation pathways of cytosine derivatives," *J. Phys. Chem. A* **118**, 9429–9437 (2014).
- <sup>50</sup>M. Merchán, R. González-Luque, T. Climent, L. Serrano-Andrés, E. Rodríguez, M. Reguero, and D. Peláez, "Unified model for the ultrafast decay of pyrimidine nucleobases," *J. Phys. Chem. B* **110**, 26471–26476 (2006).
- <sup>51</sup>J. González-Vázquez and L. González, "A time-dependent picture of the ultrafast deactivation of keto-cytosine including three-state conical intersections," *ChemPhysChem* **11**, 3617–3624 (2010).
- <sup>52</sup>A. Nakayama, Y. Harabuchi, S. Yamazaki, and T. Taketsugu, "Photo-physics of cytosine tautomers: New insights into the nonradiative decay mechanisms from MS-CASPT2 potential energy calculations and excited-state molecular dynamics simulations," *Phys. Chem. Chem. Phys.* **15**, 12322–12339 (2013).

<sup>53</sup>D. L. Barker and R. E. Marsh, "The crystal structure of cytosine," *Acta Crystallogr.* **17**, 1581–1587 (1964).

<sup>54</sup>M. G. Delcey, T. B. Pedersen, F. Aquilante, and R. Lindh, "Analytical gradients of the state-average complete active space self-consistent field method with density fitting," *J. Chem. Phys.* **143**, 044110 (2015).

<sup>55</sup>I. F. Galván, M. G. Delcey, T. B. Pedersen, F. Aquilante, and R. Lindh, "Analytical state-average complete-active-space self-consistent field nonadiabatic coupling vectors: Implementation with density-fitted two-electron integrals and application to conical intersections," *J. Chem. Theory Comput.* **12**, 3636–3653 (2016).